Proceedings of ASME Turbo Expo 2011
GT2011
June 6-10, 2011, Vancouver, British Columbia, Canada

GT2011-46038

EFFECT OF AGGRESSIVE INLET SWIRL ON HEAT TRANSFER AND AERODYNAMICS IN AN UNSHROUDED TRANSONIC HP TURBINE

Imran Qureshi[‡*], Arrigo Beretta[†], Kam Chana[‡], Thomas Povey[‡]

[‡] Department of Engineering Science, University of Oxford, Parks Road, Oxford, OX1 3PJ, UK
[†]Turbine Sub-systems, Rolls-Royce PLC, Moor Lane, Derby, DE24 8BJ, UK

ABSTRACT

Swirling flows are now widely being used in modern gas turbine combustors to improve the combustion characteristics, flame stability and reduce emissions. Residual swirl at combustor exit will affect the performance of the downstream high-pressure (HP) turbine. In order to perform a detailed investigation of the effect of swirl on a full-scale HP turbine stage, a combustor swirl simulator has been designed and commissioned in the Oxford Turbine Research Facility (OTRF), previously located at QinetiQ, Farnborough UK, as the Turbine Test Facility (TTF). The swirl simulator is capable of generating an engine-representative combustor exit swirl distributions at the turbine inlet, with yaw and pitch angles of up to +/-40 degrees.

The turbine test facility is an engine scale, short duration, rotating transonic turbine facility, which simulates engine representative M, Re, Tu, non-dimensional speed and gas-to-wall temperature ratio at the turbine inlet. The test turbine is a highly loaded unshrouded design (the MT1 turbine).

This paper presents time-averaged experimental heat transfer measurements performed on the rotor casing surface, and on rotor blade surface at 10%, 50% and 90% span. Time-averaged rotor casing static pressure measurements are also presented. Experimental measurements with and without inlet swirl are compared. The measurements are discussed with the aid of three-dimensional steady and unsteady CFD simulations of the turbine stage. Numerical simulations were conducted using the Rolls-Royce in-house code HYDRA, with and without inlet swirl.

Keywords: Transonic turbine, Heat transfer, Aerodynamics, HP rotor, Rotor casing, Combustor Swirl.

1 INTRODUCTION

Tighter aircraft emission regulations have been introduced in the last few decades, leading to considerable improvements in gas turbine combustion. Modern lean-burn combustors now use aggressive swirlers to enhance fuel-air mixing. This improves the combustion performance by stabilising the flame and reduces NO_x production by lowering peak temperatures. Considerable research in open literature concerns the effect of swirl on the combustion process. The impact of residual swirl on the flow characteristics of the downstream HP turbine has received relatively little attention. In the companion paper, Qureshi et al. [1] present a detailed experimental and computational investigation of the effects of swirl on the HP vane and endwalls. This paper presents detailed results of the impact of swirl on the aerodynamic and heat transfer characteristics of HP rotor surface and HP rotor casing.

2 REVIEW OF PAST LITERATURE

2.1 Rotor Heat Transfer - General

In a high-pressure rotating turbine, the flow in the rotor, in the tip-clearance region and on the rotor casing is highly unsteady and complex in nature. To reduce tip-leakage flow and rotor profile losses, which can account for greater than 1/3rd of the total loss (Denton [2]), robust flow predictions are required.

In early studies, casing heat transfer rate data obtained in a transient test facility under engine-representative flow conditions was reported by Guenette et al. [3] and Metzger et al. [4]. As expected, the measured heat flux reduces in the axial direction as the gas to wall temperature ratio drops through the rotor row: the result of work extraction. Polanka et al. [4] reported turbine tip and shroud heat transfer rates as high as in the stagnation region of the airfoil. Chana and Jones [6] measured the casing heat transfer rate in the presence of inlet temperature distortion and observed a reduction of casing heat load compared to the uniform inlet temperature condition. Thorpe et al. [7] evaluated true Nusselt number and corresponding adiabatic wall temperature on the casing for uniform inlet conditions. The casing heat transfer rate and

[*] Corresponding author, email: imran.qureshi@eng.ox.ac.uk

adiabatic wall temperature were found to vary significantly in the axial direction, whereas the drop in Nu was found to be less significant. Qureshi et al. [8] performed measurements with pronounced inlet temperature distortion (a profile representative of at an extreme point in the operational cycle) and reported a considerable reduction in time-averaged heat load on the rotor casing, approximately consistent with the change in adiabatic wall temperature expected at the wall with temperature distortion.

Rotor surface heat transfer studies have been performed by, for example: Guenette et al. [9] (rotor mid-span heat transfer measurements obtained in the MIT Blowdown Tunnel); Hilditch [10]; Moss et al. [11] (HP rotor heat transfer measurements obtained in the Oxford Rotor Facility); Dildier et al. [12]; Allan et al. [13]; Haldeman et al. [14].

2.2 Rotor Heat Transfer – Inlet Swirl

There is a significant amount of literature that considers the effects of swirl on combustion and emission characteristics (e.g. [15], [16], [17]) but no work (to the authors' knowledge) that considers the effect of swirl on the HP rotor or casing aerodynamic and heat transfer characteristics. It is believed that this is the first reported study in this area.

Qureshi et al. [1] discuss the possible effects that may be expected as a result of aggressive inlet swirl. These include: off-design incidence at vane inlet, resulting loading distribution changes; enhanced combustor turbulence; changes in secondary flow features and vorticity within the vane passage. Jouini et al. [18] investigated the effects of off-design flow incidence angle and observed significant changes in the loading distribution in the vicinity of the leading edge and a consequent increase in loss. Corriveau and Sjolander ([19], [20]) observed a reduction of about 20% in the total pressure losses for an aft-loaded airfoil as compared to the baseline airfoil [19]. Weiss and Fottner [21] observed a high magnitude of secondary flow loss for the front-loaded cascade.

The impact of freestream turbulence on surface heat transfer has received considerable attention. Hancock and Bradshaw [22], Blair [23], and Krishnamoorthy and Sukhatme [24] proposed correlations to estimate heat transfer enhancement with freestream turbulence. Overall, freestream turbulence has been found to augment the heat transfer and result in an earlier transition, particularly on the SS of the blade.

Qureshi et al. [1] observed a considerable increase in the vane surface heat transfer with inlet swirl: the result of additional passage vortices arising from changes in the vane loading. The effects of inlet swirl on the rotor, where the flow is dominated by the unsteady interaction with the vane potential field, wake, and secondary flow features, might be expected to be small in comparison to the vane. Particularly so as the overall level of turbulence in the rotor passage is naturally high. It is the change in the rotor heat transfer behaviour that is the subject of this paper.

3 EXPERIMENTAL FACILITY

The Oxford Turbine Research Facility (OTRF) is a short duration heat transfer facility with a full-sized high pressure research turbine stage. The main components of the facility are: i) the high pressure reservoir; ii) the pump-tube that contains a light-weight piston; iii) a fast acting plug valve; iv) the turbine stage (working section); and v) the turbobrake. These are labelled in the schematic of the research facility shown in Figure 1.

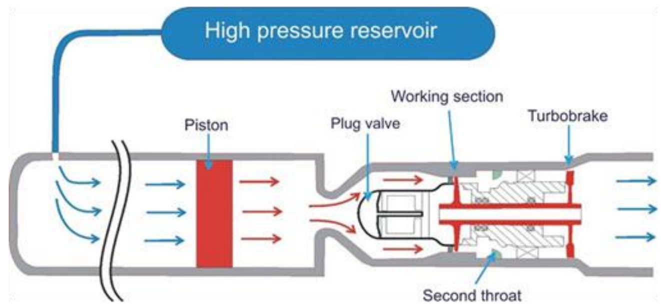

Figure 1: Schematic of Oxford Turbine Research Facility.

The operating principles of this type of facility were first described by Jones et al. [25]. Prior to an experimental run the plug valve is closed, the working section and exhaust tank are evacuated, and the turbine disc is accelerated to the design speed using an air motor. Air from the high pressure reservoir is injected into the piston tube behind the light piston. The piston moves down the piston tube acting to compress and (approximately isentropically) heat the air ahead of it. When the desired test gas conditions are achieved, the fast-acting plug valve is opened and the test gas (air) flows out of the piston tube into the large annulus. Here the gas settles before passing through the working section. The test run ends when piston reaches the end of the piston tube. Steady conditions are achieved for approximately 500 ms, during which time the experimental data are acquired. During the test period, all relevant non-dimensional parameters are matched to engine conditions. The turbobrake [26] ensures approximately constant turbine speed during the run. The OTRF has been used to test a HP turbine stage [27] and a 1.5 turbine stage [28] in the past. The operating conditions for OTRF tests are listed in Table 1.

Table 1: Turbine Stage Operating Conditions for the OTRF.

Parameter(unit)	*Nominal value*	*Allowable run-to-run variations around nominal value (%)*
p_{01} (bar)	4.6	± 1
T_{01} (K)	444	± 2
T_g/T_w	1.50	± 2
M_2^{hub}	1.054	± 1
M_2^{casing}	0.912	± 1
ω (rpm)	9500	± 1
p_{02rel} (bar)	2.697	± 1

The working section of OTRF is shown in Figure 2 The test turbine (MT1) stage has 32 NGVs and 60 rotor blades. The stage total-to-static pressure ratio is 3.2. The NGV true chord and the exit swirl angle are 70.1 mm and 74.4º at mid-span location. The vane has an aspect ratio of 0.53 and an exit Reynolds number of 2.6 x 10^6. For current investigation, the test facility was upgraded with the installation of an inlet swirl generator, which is briefly described in the next section.

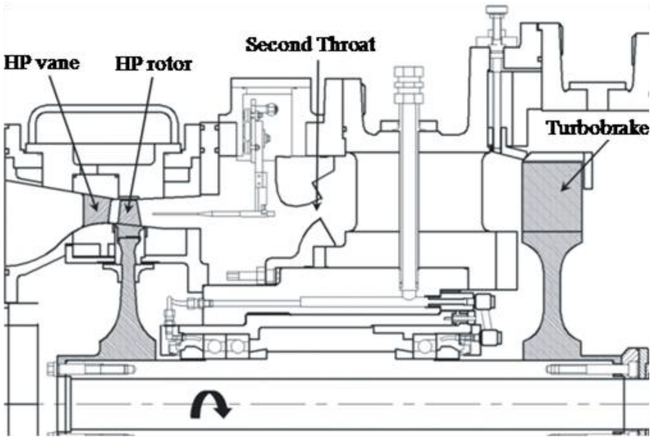

Figure 2: The working section of the OTRF with the HP turbine stage and turbobrake highlighted.

4 INLET SWIRL SIMULATOR

In order to carry out detailed experimental investigations of the effects of swirl on the HP turbine stage, an inlet swirl simulator has been designed and commissioned in the OTRF. The target swirl profile at the turbine stage inlet is typical of a swirled combustor design, with peak yaw and pitch angles of up to +/-40 degrees. The development, installation and commissioning of the swirl simulator in the OTRF is discussed in detail by Qureshi and Povey [29].


Figure 3: The assembled inlet swirl simulator module.

The swirl simulator module was designed to mount in the tunnel flow path upstream of the OTRF inlet contraction. The module allows for rotation so that clocking of the vortex core with respect to the NGV leading edge could be achieved. To aid in CFD comparison, and to allow repeatability assessment around the annulus, an integer swirler to vane count ratio of 1:2 was chosen (16 swirlers and 32 NGVs). The manufactured swirl generation system, about 1 m in diameter, is shown in Figure 3. Each swirler is composed of six flat-plate vanes inclined at an angle of 40º to the axial direction. The flow conditions measured at the inlet of HP turbine with inlet swirl are presented in section 5.

5 INLET CONDITIONS WITH SWIRL

Inlet swirl profile measurements were performed using rakes of four-hole probes 0.7 axial chords upstream of the vane leading edge, the details of which are provided in [29]. The inlet area survey covered one swirler pitch (equivalent to 2 NGV pitches). Measured pitch angle (β) and yaw angle (α) distributions are presented in Figure 4 and Figure 5 respectively: circular dots indicate the points at which measurements were conducted. At some points it was not possible to reduce the data using the calibration maps because of the extreme compound flow angles. The data have been extrapolated to the wall in the regions nearest to the hub and casing. The general distribution of pitch and yaw angles corresponds to a well defined clockwise vortex (as viewed from upstream) of approximately the desired magnitude.

The vortex is more easily visualised with flow vectors, as shown in Figure 6, which has been obtained using the secondary flow velocity components at each measurement point. To aid visualisation, data has been interpolated for the internal missing points and extrapolated for the points at 10% and 90% radial span. The thick arrows represent the measured locations in the plot.

The yaw angle profile measured in the OTRF is compared with the target profile in Figure 7. Results are presented at 20% and 80% span. The measured peak yaw magnitude (approximately 50 degrees) is well over the target value indicating a well-formed clockwise vortex as desired.

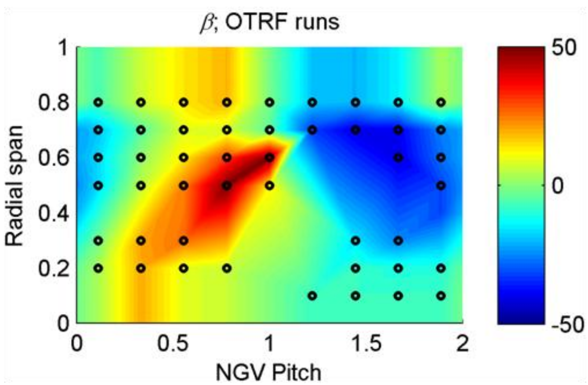

Figure 4: Pitch angle profile measured at 0.7 C_{ax} upstream of NGV inlet with swirl (circles represent measurement points).

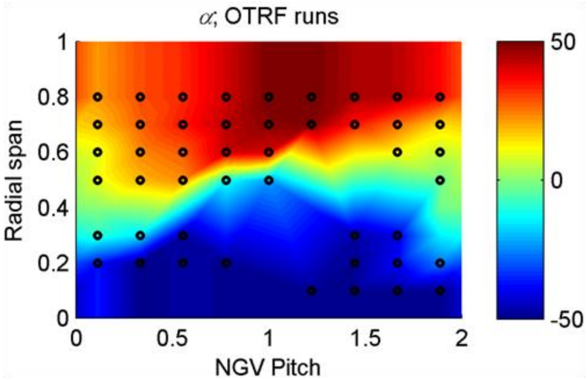

Figure 5: Yaw angle profile measured at 0.7 C_{ax} upstream of NGV inlet with swirl (circles represent measurement points).

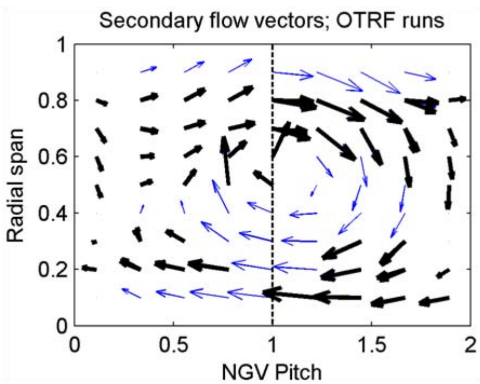

Figure 6: Measured secondary flow vectors at 0.7 C_{ax} upstream of NGV inlet with swirl viewed from upstream (bold arrows represent measurement points; thin arrows are interpolated/extrapolated).

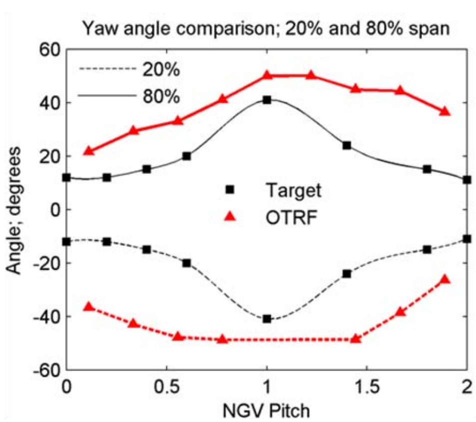

Figure 7: Yaw angle profile at 20% and 80% span; comparison of measurements in the OTRF with the target profile.

Inter-stage area-survey measurements were not performed in the present study. The flow at inlet to the rotor is considered by examining the predicted flowfield at the rotor inlet plane. A comparison of the predicted and measured vane loading distributions with and without inlet swirl [1] shows good agreement between CFD and experiment.

The circumferentially-averaged vane exit static pressure and Mach number distributions are shown in Figure 8(a) and Figure 9(a), for uniform inlet conditions and for inlet swirl. The corresponding percentage changes are shown in Figure 8(b) and Figure 9(b).There is a decrease in static pressure at vane exit which is more pronounced towards the casing. The span averaged decrease is about 0.85 %. There is a corresponding increase in Mach number with swirl (see Figure 9(b)) of 0.83%, on average. A maximum local increase of 1.5% was predicted at 90% span.

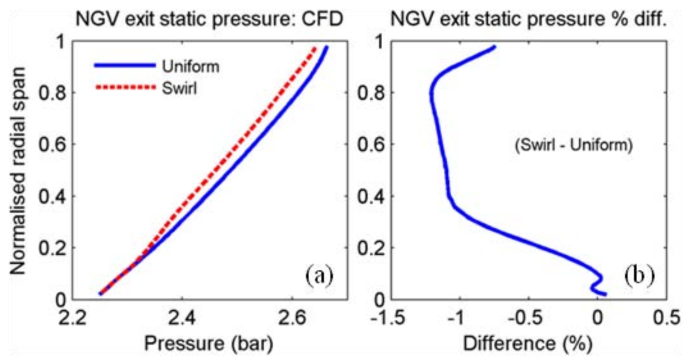

Figure 8: (a) Predicted NGV exit static pressure distribution for uniform inlet and swirl; (b) percentage difference with swirl.

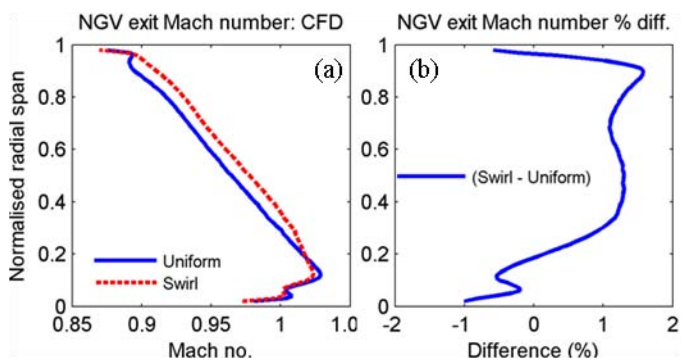

Figure 9: (a) Predicted NGV exit Mach number distribution with uniform inlet and swirl; (b) percentage difference with swirl.

At a nominal vane exit Mach number of 0.95, for isentropic flow the gradient dM/dp = -0.93. The percentage change in exit Mach number (Figure 9(b)) is comparable with the change in static pressure (Figure 8(b)), implying a decrease in total pressure loss with swirl of approximately 0.1%. This is consistent with the total pressure distributions at vane exit presented in Figure 10. Over most of the span there is a decrease in total pressure loss with swirl of between 0.1% and 0.4%, an effect that is perhaps expected as the result of general off-loading of the vane (the combined effect of the vortices is circulation around the axis in the same direction as the swirl introduced by the vanes). The reduction in total pressure loss in the midspan region is counteracted by significant increases in total pressure loss in the hub and casing regions. There is an increase in total pressure loss of up to 0.6% in the hub region where vane loading is increased.

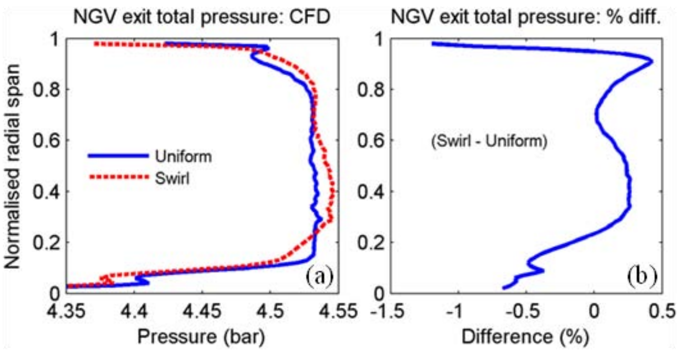

Figure 10: (a) Predicted NGV exit total pressure for uniform inlet and swirl; (b) percentage difference with swirl.

The decrease in inter-stage static pressure also implies a redistribution of stage capacity, that is, a relative decrease in the ratio of NGV and rotor capacity. This is likely to be associated with highly swirling flow in the NGV passage, which would cause a reduction in NGV capacity.

The vane exit whirl angle is significantly affected by inlet swirl as shown in Figure 11. There is an increase in vane exit whirl angle of approximately 1º (on average) above 40% span, and a decrease of up to 3º below 30% span. This change in vane exit whirl angle and the change in inter-stage static pressure, cause a change in the rotor relative inlet conditions.

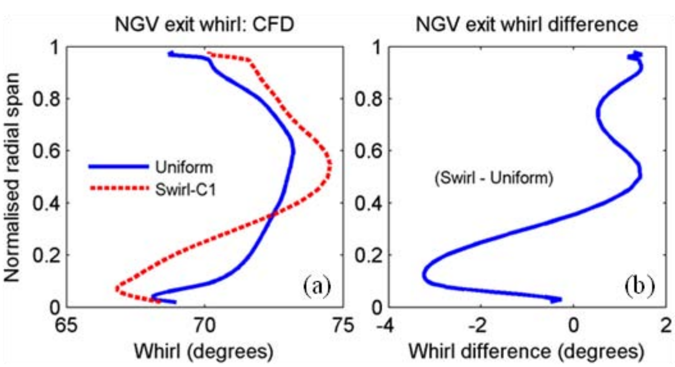

Figure 11: (a) Predicted vane exit whirl angle distribution with uniform inlet and swirl; (b) percentage difference with swirl.

.

Figure 12(a) and Figure 12(b) compare the predicted rotor relative inlet whirl angle with and without swirl. Above 35% span an increase in incidence by up to 4º is observed. Below 35% span, negative incidence of up to 6º is observed. The incidence angle changes are consistent with a clockwise vortex being propagated into the rotor row. As expected, in the highly accelerated flow at the rotor inlet plane, the variation in whirl angle caused by swirl is less significant than at the NGV inlet plane.

Figure 13(a) compares the predicted rotor relative inlet total pressure for the two cases. A decrease in total pressure is observed with swirl above 35% span, and an increase between 10% and 35% span. Figure 13(b) presents the percentage difference in total pressure with swirl, which varies between +1.8% and –2%. This change in total pressure might be expected to drive additional secondary flows. The pronounced local maximum in total pressure centred on approximately 20% span, which is not accompanied by a peak in swirl, causes significant streamline divergence on the PS of the vane at the same span location – see Figure 32. Figure 14(a) compares the rotor relative inlet Mach number and Figure 14(b) presents the corresponding percentage difference for the two cases.

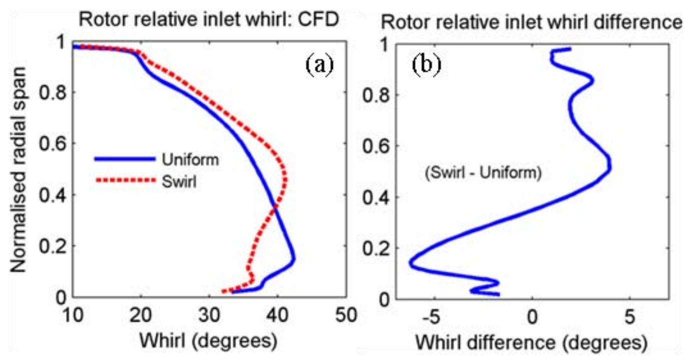

Figure 12: (a) Predicted rotor relative inlet whirl angle with uniform inlet and swirl; (b) percentage difference with swirl.

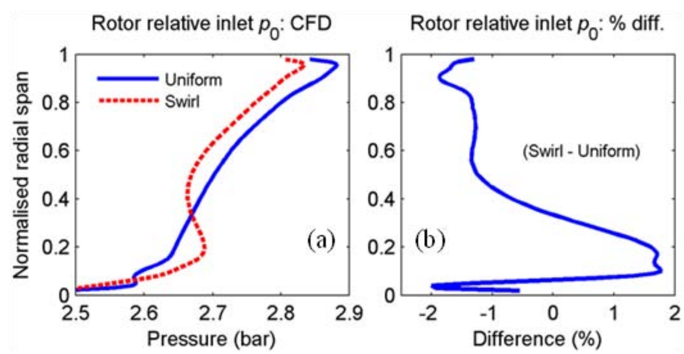

Figure 13: (a) Predicted rotor relative inlet total pressure with uniform inlet and swirl; (b) percentage difference with swirl.

Examining the exit relative total pressure distributions presented in Figure 15 shows significant differences in loss through the rotor passage. There is a decrease in loss in the hub region, where a reduction in incidence reduces the loading on the blade. The most pronounced difference in the tip region, where there is a significant increase in loss (more than 1% additional loss) in the 90% to 100% span region, even taking into account the reduction in rotor relative inlet total pressure in this region. This increase in total pressure loss appears to be associated with increased incidence in the tip region. Positive incidence leads to increased loading of the tip, and a tendency for greater flow through the tip gap. This appears to be supported by the streamline pattern presented in Figure 32, but will be the subject of further analysis.

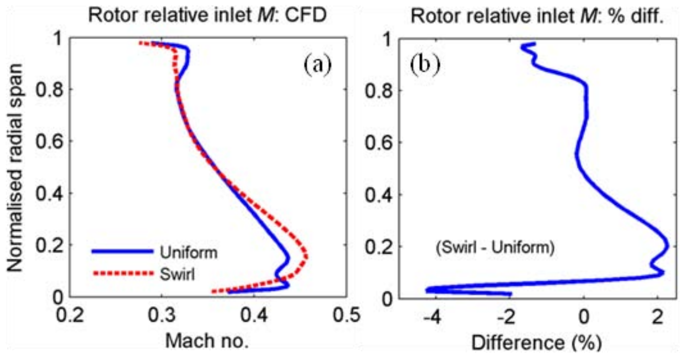

Figure 14: (a) Predicted rotor relative inlet Mach number with uniform inlet and swirl; (b) percentage difference with swirl.

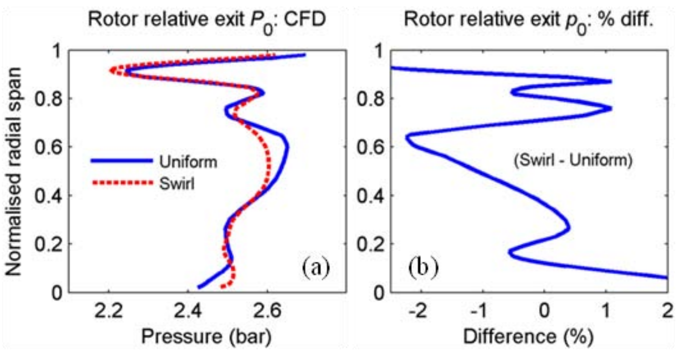

Figure 15: (a) Predicted rotor relative exit total pressure with uniform inlet and swirl; (b) percentage difference with swirl.

6 EXPERIMENTAL INSTRUMENTATION AND DATA REDUCTION

Heat transfer measurements were conducted on the HP rotor and casing surfaces using thin film gauges. The rotor casing static pressure field was also measured. A brief description of the instrumentation and data processing is given below.

6.1 Rotor Casing Pressure Measurements

Time-averaged static pressure measurements were conducted on the rotor casing using a cassette with 57 flush mounted pneumatic tappings. The tappings were fitted in rows at an angle of 52º to the axial, approximately following the stagger angle of the rotor blade. The tappings covered approximately 2 NGV pitches circumferentially, and were distributed over one rotor axial chord.

6.2 Rotor Casing Heat Transfer Measurements

Thin-film platinum resistance heat transfer gauges were used to measure heat flux on the rotor casing. The gauges were deposited on Kapton™ (polyamide) bonded to a Perspex casing cassette. A set of four cassettes was used (~20 gauges per cassette) providing a composite map of approximately 80 measurement points. The measurements covered approximately 2 NGV pitches in the circumferential direction and the rotor axial chord in the axial direction. Heat transfer electrical analogue (HTA) circuits [30] were used to directly measure heat flux data during a test. Using the measured heat flux data, the temperature signal was reconstructed for each gauge as described in Oldfield et al. [31]. During a run, the heat flux drops with time as the surface temperature rises. The surface temperature rises by up to 60ºC allowing a regression of heat flux against surface temperature to obtain local adiabatic wall temperature [31]. The adiabatic wall temperature, T_{aw}, was used to reduce the heat flux data to Nusselt number, based upon the rotor true chord, C, using the relation given in Eq. (1). The thermal conductivity of air, k, was evaluated at the mean inlet total temperature. The regression to achieve T_{aw} was relatively stable for a run, as shown by the sample plots in Figure 16 for one gauge.

$$Nu = \frac{\dot{q}C}{(T_{aw} - T_w)k} \tag{1}$$

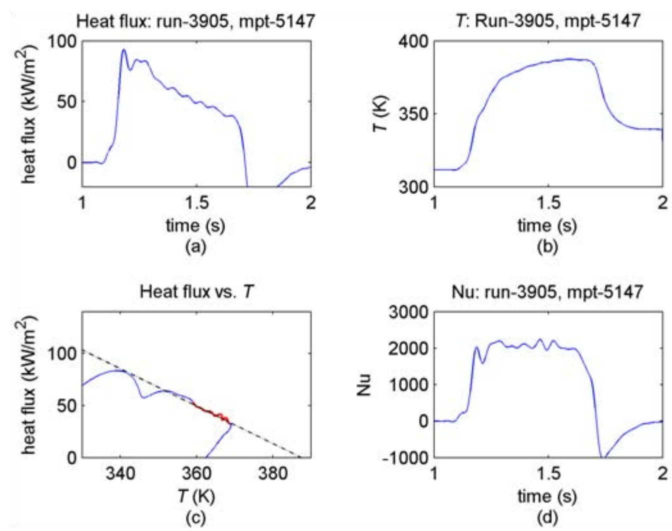

Figure 16: (a) Measured heat flux for typical run; (b) Temperature reconstructed from measured heat flux; (c) Heat flux plotted against reconstructed temperature to obtain T_{aw} by regression; (d) Nusselt number.

6.3 Rotor Surface Heat Transfer Measurements

Heat transfer measurements were obtained on the rotor surface at 10%, 50% and 90% span using platinum resistance thin film gauges with two-layered substrate: an insulating layer of Kapton on a (thermally) semi-infinite layer of metal. The theory for the use of multi-layered gauges is given in Doorly and Oldfield [32]. To minimise the effects of slip-ring noise, the signals were high-frequency boosted using an in-shaft pre-amplifier. The natural temperature signal was recovered by de-boosting the signal in post-processing. The heat flux was evaluated from the measured surface temperature by using Fast Fourier Transform technique [33]. The surface temperature rise in the rotor relative frame during the steady part of the run is not sufficient to accurately apply the regression technique for local adiabatic wall temperature. The measured heat flux data was reduced to Nusselt number using the rotor relative inlet total temperature, using Eq. (2). The rotor relative inlet total temperature was calculated from the design velocity triangles at each span.

$$Nu_{T02rel} = \frac{\dot{q}C}{(T_{02rel} - T_w)k_{T02rel}} \tag{2}$$

6.4 Measurement Uncertainty

A detailed treatment of the uncertainty related to the heat transfer measurements in the transient turbine experiment environment is provided by Povey [34]. In the current study the resulting precision and absolute uncertainties for uniform inlet and swirl are presented in Table 2.

Table 2: Measurement Precision and Absolute Uncertainty

Variable	*Precision*		*Absolute Uncertainty*	
	Uniform	Swirl	Uniform	Swirl
T_0	± 1 K	± 3 K	± 5 K	± 7 K
T_w	± 1.5 K	± 1.5 K	± 1.5 K	± 1.5 K
$\dot{q}$	1.5%	1.5%	3.4%	3.4%
T_{aw}	± 1 K	± 3 K	± 5 K	± 7 K
Nu	1.9%	3.6%	5.6%	7.6%

7 NUMERICAL SIMULATIONS

Three-dimensional computational simulations were conducted with and without inlet swirl. The measured values of pitch and yaw (Figure 4 and Figure 5) were used as inlet boundary conditions for the simulations with swirl.

Each swirler covered 2 NGV pitches, so a structured computational grid comprising 2 NGVs and 4 rotor blades (actual vane/blade count is 32/60), was developed using the Rolls-Royce in-house tool PADRAM. The mesh used ~5 million cells. The rotor airfoils were skewed to reproduce the rotor capacity of the original geometry. The Rolls-Royce in-house CFD solver HYDRA was used. This employs an efficient edge-based data structure, as described by Moinier and Giles [35]. A MUSCL based flux-differencing algorithm is used to integrate the flow equations around median-dual control volumes. Block Jacobi pre-conditioning of the discrete flow equations is applied [36] and a 5-stage Runge-Kutta scheme is employed for convergence of the steady state solution [37]. An element-collapsing multi-grid algorithm is used to accelerate the convergence to steady state [38]. Nonlinear unsteady calculations were performed using implicit dual time-stepping.

Both steady and unsteady solutions were obtained. Unsteady solutions were time-averaged for comparison with steady solutions. The Spalart-Allmaras turbulence model was implemented with wall functions. For each case, two solutions were obtained at two isothermal wall temperatures, T_{w1} and T_{w2}, allowing heat transfer coefficient to be determined from the heat fluxes using Eq. (5). Adiabatic wall temperature was obtained by substituting heat transfer coefficient in either Eq. (3) or Eq. (4).

$$\dot{q}_1 = h(T_{aw} - T_{w1}) \tag{3}$$

$$\dot{q}_2 = h(T_{aw} - T_{w2}) \tag{4}$$

$$h = \frac{(\dot{q}_1 - \dot{q}_2)}{(T_{w2} - T_{w1})} \tag{5}$$

8 RESULTS AND DISCUSSION – ROTOR CASING

8.1 Rotor Casing Static Pressure Results

The results obtained from the time-averaged static pressure measurements on the rotor casing are presented in Figure 17. Measurements obtained with and without inlet swirl are presented for comparison. The dots indicate the points where the measurements were obtained. The potential field effect of the NGVs reduces with axial distance. The casing static pressure drops from a value of about 2.8 bar at the rotor inlet to a value of about 1.4 bar at the rotor exit. The results are similar in form for the two cases. Corresponding time-averaged static pressure results on the rotor casing, obtained from unsteady numerical predictions, are presented in Figure 18. The form of the distribution is broadly similar to the experimental results.

A comparison of the circumferentially-averaged data is performed in Figure 19. The results cover approximately a rotor chord. The general trend is similar for all data sets. For the experimental data, however, there is a significant difference between the data for swirl and uniform conditions from approximately 68 mm to the rotor exit plane ~77 mm. There is an increase in static pressure with inlet swirl by between 3 and 6 %.

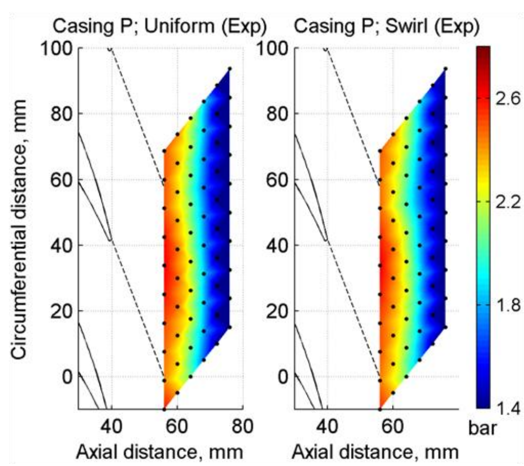

Figure 17: Measured rotor casing static pressure distribution with uniform inlet and with inlet swirl.

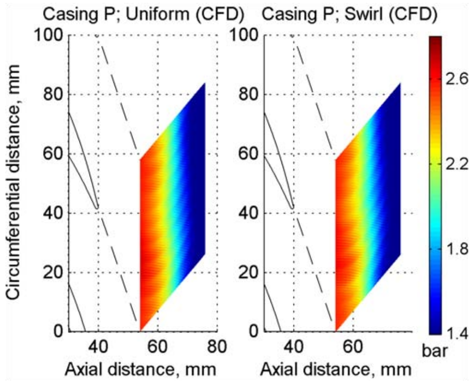

Figure 18: Predicted rotor casing static pressure distribution with uniform inlet and with inlet swirl.

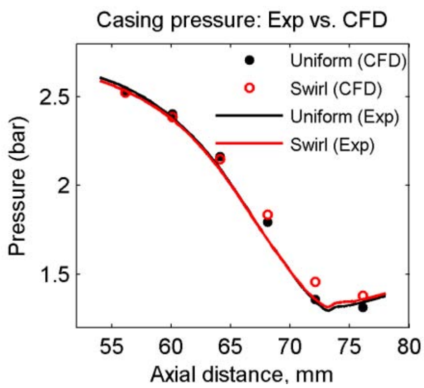

Figure 19: Circumferentially averaged rotor casing static pressure: comparison of measured and predicted distributions.

8.2 Experimental Rotor Casing Heat Transfer Results

Time-averaged heat transfer measurements performed on the rotor casing with uniform inlet temperature are presented in Figure 20. The data were acquired as part of an earlier programme using the same instrumentation as used for the current programme (Chana and Jones [6]).

Figure 20(a) shows the measurement points and also the triangular grid used for interpolation. Using the regression technique (section 6.2), the measured heat flux and wall temperature trends with time (over a steady period of around 250 ms of the run) were used to evaluate adiabatic wall temperature at each gauge location. Figure 20(c) presents an area plot of the adiabatic wall temperature. T_{aw} drops from approximately 410 K at rotor inlet to 320 K at the rotor exit due to work extraction though the rotor passage. The evaluated driving gas temperature ($T_{aw} - T_w$) was used to reduce the heat flux data to Nusselt number i.e. Nu(t). Figure 20(b) presents the plot of Nu, time-averaged over the steady part of the run. There is significant non-uniformity in Nu in both the axial and circumferential directions. Peaks are observed just downstream of rotor inlet plane, where the loading on the rotor is highest, and where tip leakage velocities above the crown are highest. The peaks are aligned with the direction of vane wakes suggesting that high Tu levels in the wake promote higher Nu.

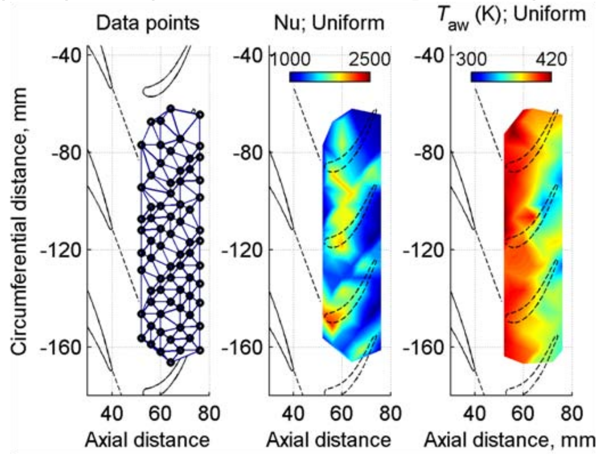

Figure 20: Rotor casing heat transfer measurements for uniform inlet conditions: (a) Measurement points and interpolation grid; (b) Area plot of Nu; (c) Area plot of computed T_{aw}.

For the case of inlet swirl, alternate vanes leading edges were geometrically aligned with the centres of the upstream swirlers. The vane aligned with vortex centre is termed C1. The vane aligned between vortex centres is termed C2. Two sets of casing heat transfer measurements were obtained centred on wakes from a vane C1 and a vane C2. These casing positions are termed C1-C2 and C2-C1. This is shown schematically in Figure 21. In the experiments, the second set of data was obtained using the same casing heat transfer instrumentation, by clocking the upstream swirler plate by one NGV pitch in the clockwise direction.

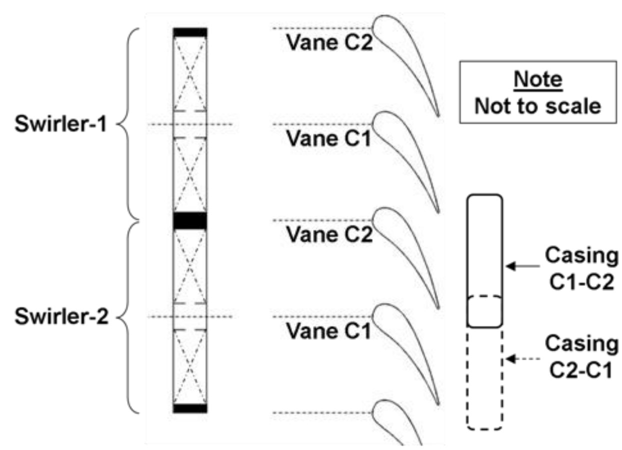

Figure 21: HP rotor casing measurement cassette, geometric alignment with respect to upstream vanes and swirlers.

Figure 22 and Figure 23 present the measured results for casing heat transfer with inlet swirl for C1-C2 and C2-C1 respectively. The measured heat flux and wall temperature data have been used to compute Nu and T_{aw}. The general trends for

C1-C2 and C2-C1 are similar. The gross trends in Nu and T_{aw} are also similar to the case for uniform inlet flow: the local effects of swirl are limited in this region. This is perhaps to be expected because the casing region is dominated by the unsteady interaction with the flow over the rotor tip. There is a modest increase in both the circumferentially averaged Nu and T_{aw} with inlet swirl, which is discussed subsequently.

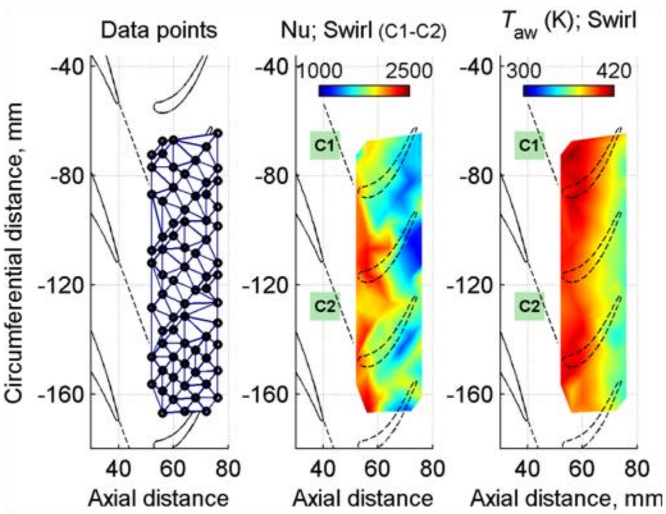

Figure 22: Rotor casing heat transfer measurements with inlet swirl, passage C1-C2: (a) Measurement points and interpolation grid; (b) Area plot of Nu; (c) Area plot of computed T_{aw}.

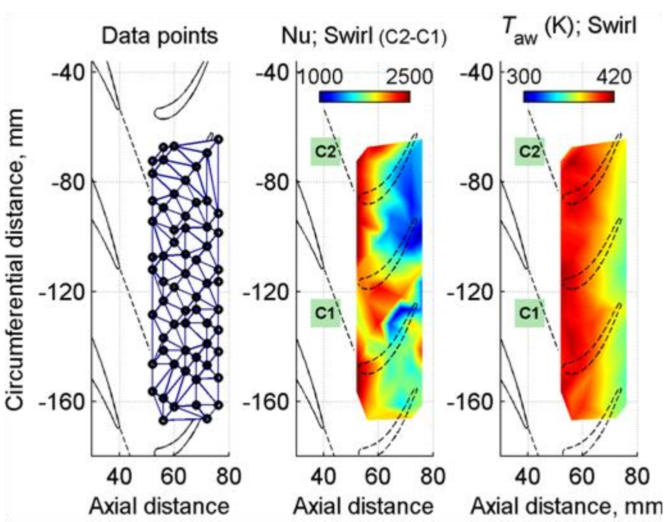

Figure 23: Rotor casing heat transfer measurements with inlet swirl, passage C2-C1: (a) Measurement points and interpolation grid; (b) Area plot of Nu; (c) Area plot of computed T_{aw}.

8.3 Computational Rotor Casing Heat Transfer Results

Numerical solutions were obtained for uniform inlet and for inlet swirl cases. For each case, two heat flux solutions were obtained at different wall temperatures to compute heat transfer coefficient. The time-averaged Nu and T_{aw} for the two cases, obtained from instantaneous unsteady solutions (10 time steps), are compared in Figure 24 and Figure 25 respectively. The area plots extend NGV pitches in the circumferential direction and from rotor inlet to exit in the axial direction.

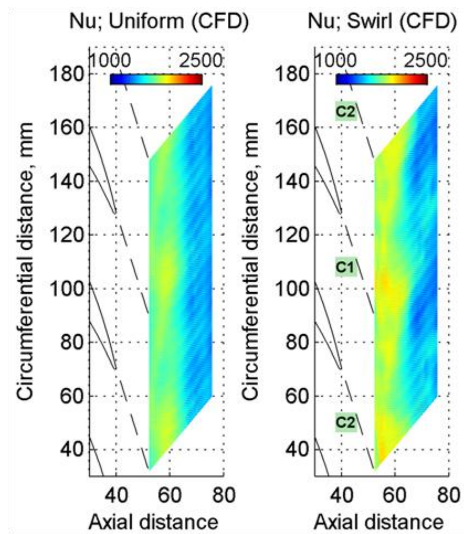

Figure 24: Rotor casing predicted Nu: (a) Uniform; (b) Swirl.

The general trends are similar for the uniform inlet flow and the swirl cases. A small circumferential variation with NGV pitch is seen in both Nu and T_{aw} results. This is broadly consistent with the experimental results, and expected as the result of the potential field and wake interaction with the rotor. A slight increase in Nu is observed with swirl.

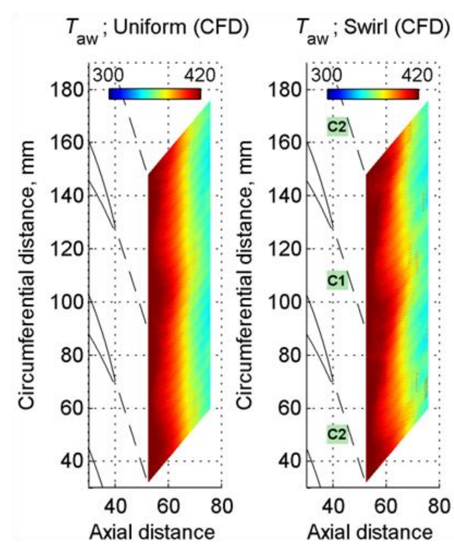

Figure 25: Rotor casing predicted T_{aw} (K): (a) Uniform; (b) Swirl.

The circumferential average values of Nu and T_{aw} are presented in Figure 26 and Figure 27, and compared to experimental results.
Both the experiment and prediction show an increase in Nu with inlet swirl. A greater increase is observed in experiments than predictions, however: a mean increase of 20% was measured, compared to a 3% increase in the prediction. The agreement between the predicted and measured T_{aw} (Figure 27) was reasonably good, with slightly higher values in the CFD simulations than in the experiment.

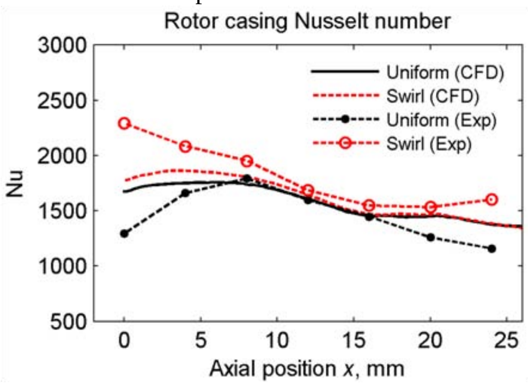

Figure 26: Circumferentially averaged Nu on rotor casing.

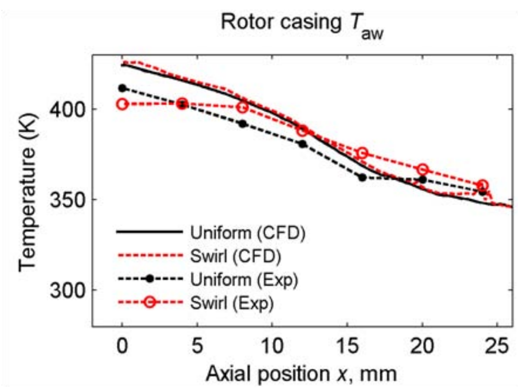

Figure 27: Circumferentially averaged T_{aw} on rotor casing.

9 RESULTS AND DISCUSSION – ROTOR SURFACE

Rotor surface heat transfer measurements were conducted at 10%, 50% and 90% span with uniform inlet conditions and also with inlet swirl. Between 5 and 8 gauges were used on each surface (PS or SS) at a given span location. The measured heat flux and wall temperature data was processed to Nu as described in section 6.3. Measured Nu distributions are presented in Figure 28, Figure 29 and Figure 30, for 10, 50 and 90% span respectively. Results for both uniform and swirl cases are compared. Data could not be obtained at the mid-span PS for the uniform case as the instrumentation was damaged.

The similarity of the results with and without swirl is striking, and is in contrast to the results for the NGV surfaces: Qureshi et al. [1] measured an enhancement of over 100% in mid-span Nu with swirl. This is perhaps not unexpected in an environment dominated by unsteady interactions with, for example, highly turbulent vane wakes. The acceleration in the NGV passage also causes the effects of the swirl to be reduced.

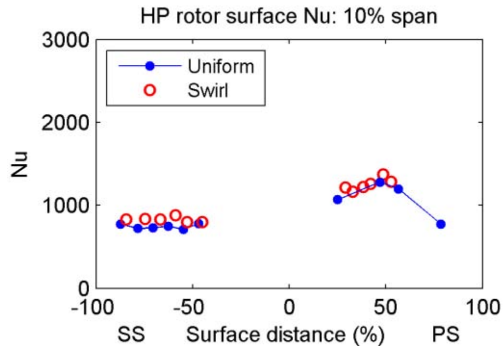

Figure 28: Measured HP rotor surface Nu at 10% span.

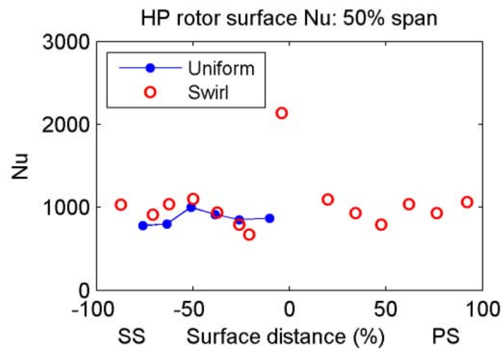

Figure 29: Measured HP rotor surface Nu at 50% span.

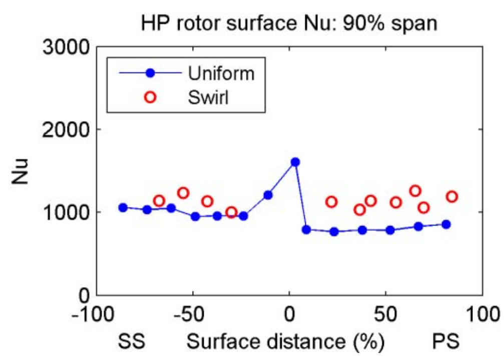

Figure 30: Measured HP rotor surface Nu at 90% span.

At all span locations on the SS an enhancement ranging from 7 to 13% was observed with swirl. This is likely the result of increased freestream turbulence. The predicted flow pattern on the SS of the rotor blade is very similar for both uniform conditions and inlet swirl. This is illustrated in Figure 31. The measured freestream turbulence intensity at the NGV inlet plane for uniform inlet conditions was 6.5% (Chana,[39]). Beard [40] measured the turbulence intensity with inlet swirl as 11.2%.

The most significant change in Nu was observed on the PS at 90 % span, where the enhancement was approximately 40%. A possible explanation is the increased tip leakage flow, driven by higher incidence in the tip region and therefore higher loading at the tip, which causes a change in the streamline pattern at approximately 90% span. This is illustrated with the surface streamlines shown in Figure 32.

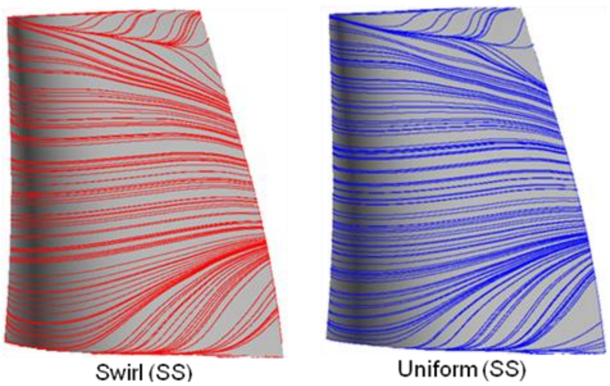

Figure 31: Comparison of predicted rotor SS flow pattern for uniform inlet and swirl.

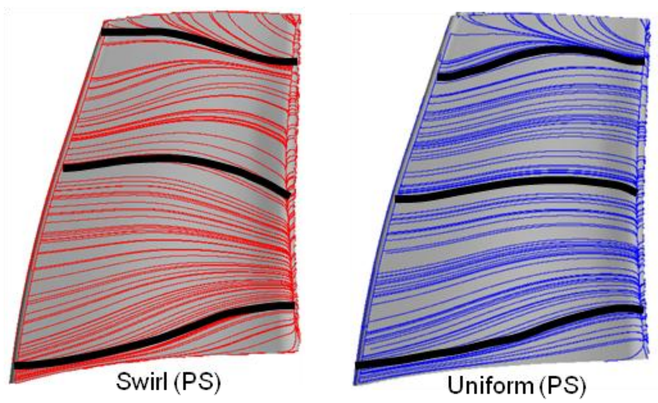

Figure 32: Comparison of predicted rotor PS flow pattern for uniform inlet and swirl.

Swirl causes significant redistribution of the rotor PS fluid, as shown in Figure 32. The bold lines emanating from 10%, 50% and 90% span at the leading edge follow different paths in the simulations with uniform inlet flow and with inlet swirl. At 10% span the effect is very small: there is very slight downward migration of flow. At 50% span there is significant upward migration of flow. This is associated with a wide region between 15% and 50% span in which streamline divergence is caused in the case of inlet swirl by a local maximum in rotor relative total pressure (see Figure 13) at approximately 20% span. At 90% span it appears that more fluid is swept over the tip of the blade for the case of inlet swirl – a result that would be consistent with the greater loading caused by positive incidence in this region.

10 CONCLUSIONS

A detailed experimental and computational investigation of the effect of high inlet swirl on the heat transfer characteristics of a HP rotor and casing has been conducted. Experiments were performed in a rotating transonic turbine facility, which was modified to incorporate an inlet swirl generator which replicated typical low-NOx combustor exit conditions. It is believed that this is the first comprehensive study of this kind.

The computational results highlight changes in vane exit whirl angle and total pressure profiles with inlet swirl, which cause a change in the rotor relative inlet whirl and total pressure fields. The changes in rotor relative incidence angle changes are consistent with a clockwise vortex being propagated into the rotor row. As expected, the variations in rotor whirl angle are less significant than those observed at the NGV inlet plane with inlet swirl [1].

Heat transfer measurements on the rotor casing for two different clocking positions of the upstream swirl centre (with respect to the vane) show little sensitivity of casing heat transfer and adiabatic wall temperature profiles to swirl clocking position. In both cases, an area mean increase in Nusselt number of about 20% was observed with inlet swirl. Similar trends were observed in computational simulations but the predicted change was less than measured experimentally.

Heat transfer measurements obtained at three span-wise locations on the rotor surface indicate the effect of swirl on the rotor is less significant than on the NGV, although an increase in rotor surface Nusselt number was observed with inlet swirl. An increase of between 7 and 13% was observed on the rotor SS, which may be due to enhanced turbulence intensity with inlet swirl. On the PS, an increase of about 8% (at 10% span) to 40% (at 90% span) is observed, which appears to result from the combined effect of enhanced turbulence and increased secondary flows with swirl, causing greater tip leakage flow and greater attendant streamline divergence in the tip region.

11 NOMENCLATURE

Romans and Greeks

α	Yaw angle, degrees
β	Pitch angle, degrees
C	NGV midspan true chord, mm
ρ	Density, Kg/m^3
h	Heat transfer coefficient
k	Thermal conductivity
M	Mach number
Nu	Nusselt number
p	Pressure, bar
$\dot{q}$	Heat flux, kW/m^2
T	Temperature, K
T_{aw}	Adiabatic wall temperature, K
T_g	Gas temperature, K
T_w	Wall temperature, K
u	Velocity, m/s^2

ω	Turbine speed (rpm)
x	Axial distance (mm)

Subscripts, superscripts, abbreviations

0	Total (absolute)
1	NGV inlet plane
2	NGV exit plane
a, ax	Axial distance
rel	Rotor relative
Exp	Experimental
OTRF	Oxford Turbine Research Facility
TTF	Turbine Test Facility
HP	High Pressure
HTA	Heat Transfer Analogue
NGV	Nozzle Guide Vane
Tu	Turbulence
PS, SS	Pressure side, Suction side
LE, TE	Leading edge, Trailing edge
MUSCL	Monoton Upstream-centred Scheme for Conservation Laws
C1	Position (or vane LE) aligned with vortex centre
C2	Position (or vane LE) aligned with centre of 2 vortices

12 ACKNOWLEDGMENTS

The authors would like to acknowledge the financial support provided by the EC for the TATEF II Project, and the QinetiQ staff who supported experiments at QinetiQ Farnborough.

13 REFERENCES

[1] Qureshi, I., Smith, A. D., Povey, T., 2011, "HP Vane Aerodynamics and Heat Transfer in the Presence of Aggressive Swirl," Proc. ASME IGTI Turbo Expo 2011. Paper No. 2011-GT-46037.

[2] Denton, J. D., 1993, "Loss Mechanisms in Turbomachines," ASME J. of Turbo., Vol. 115, pp. 621–656.

[3] Guenette, G. R., Epstein, A. H., Norton, R. J. G., Yuzhang, C. 1985, "Time-Resolved Measurements of a Turbine Rotor Stationary Tip Casing Pressure and Heat Transfer Field," AIAA Paper No. 85-1220.

[4] Metzger, D. E., Dunn, M. G., Hah, C., 1991, "Turbine Tip and Shroud Heat Transfer," Trans. of the ASME. J. of Turbo. Vol. 113, pp. 502-507.

[5] Polanka, M. D., Hoying, D. A., Meininger, M., MacArthur C. D., 2003, "Turbine Tip and Shroud Heat Transfer and Loading – Part A: Parameter Effects including Reynolds Number, Pressure Ratio, and Gas-to-Metal Temperature Ratio," J. of Turbo. Vol. 125, pp. 97-106.

[6] Chana, K. S., Jones, T. V., 2003, "An Investigation on Turbine Tip and Shroud Heat Transfer," J. of Turbo. 125, pp. 513-520.

[7] Thorpe, S. J., Yoshino, S., Ainsworth, R. W., Harvey, N. W., 2004, "An Investigation of the Heat Transfer and Static Pressure on the Over-tip Casing Wall of an Axial Turbine operating at Engine Representative Flow Conditions. (I). Time-mean Results," Int. J. of Heat and Fluid Flow 25. pp 933–944.

[8] Qureshi, I., Smith, A. D., Chana, K. S., Povey, T., 2010, "Effect of Temperature Nonuniformity on Heat Transfer in an Unshrouded Transonic HP Turbine: An Experimental and Computational Investigation," Proceedings of ASME Turbo Expo 2010, Paper No. 2010-GT-22700.

[9] Guenette, G. R., Epstein, A. H., Giles, M. B., Haimes, R., and Norton, R. J. G., 1988, "Fully Scaled Transonic Turbine Rotor Heat Transfer Measurements," ASME J. of Turbo. 111, pp. 1-7.

[10] Hilditch, M. A., 1989, "Unsteady Heat Transfer Measurements in a Rotating Gas Turbine Stage," D.Phil Thesis, Department of Engineering Science, University of Oxford.

[11] Moss, R. W., Sheldrake, C. D., Ainsworth, R. W., Smith, A. D., and Dancer, S. N., 1995, "Unsteady Pressure and Heat Transfer Measurements on a Rotating Blade Surface in a Transient Flow Facility," 85th Propulsion and Energetic Panel Symposium on Loss Mechanism and Unsteady Flows in Turbomachines, Derby, UK, 1995. AGARD CP No. 571.

[12] Didier, F. Denos, M., Arts, T. 2002, "Unsteady Rotor Heat Transfer in a Transonic Turbine Stage," Transactions of the ASME. Vol. 124, pp. 614-622.

[13] Allan, W. D., Ainsworth, R., Thorpe, S. 2008, "Unsteady Heat Transfer Measurements from Transonic Turbine Blades at Engine Representative Conditions in a Transient Facility," J. Eng. Gas Turbines Power, Vol. 130, 041901-1-12.

[14] Haldeman, C. W., Mathison, R. M., Dunn, M. G., Southworth, S. A., Harral, J. W., Heltland, G. 2008, "Aerodynamic and Heat Flux Measurements in a Single-Stage Fully Cooled Turbine – Part II: Experimental Results," ASME. J. of Turbo. Vol. 130. Issue 2.

[15] Gupta, A.K., Lewis, M.J., Daurer, M., 2001, "Swirl effects on combustion characteristics of premixed flames," J. Eng. Gas Turbines Power, 123, pp.619-626.

[16] Li, G., Gutmark, E.J., 2004, "Effects of swirler configurations on flow structures and combustion characteristics," ASME Paper No. GT2004-53674.

[17] Huang, Y., Yang, V., 2005, "Effects of swirl on combustion dynamics in a lean-premixed swirl-stabilized combustor," Proc. of combustion institute, 30, pp.1775-1782.

[18] Jouini, D. B. M., Sjolander, S. A., Moustapha, S. H., 2001, "Aerodynamic Performance of a Transonic Turbine Cascade at Off-Design Conditions," ASME J. Turbomachinery, Vol. 123, pp. 510-518.

[19] Corriveau, D., Sjolander, S. A., 2004, “Influence of Loading Distribution on the Performance of Transonic High Pressure Turbine Blades,” ASME J. Turbomachinery, Vol. 126, pp. 288-296.

[20] Corriveau, D., Sjolander, S. A., 2007, “Influence of Loading Distribution on the Off-Design Performance of High Pressure Turbine Blades,” ASME J. Turbomachinery, Vol. 129, pp. 563-571.

[21] Weiss, A. P., Fottner, L., 1995, “The Influence of Load Distribution on Secondary Flow in Straight Turbine Cascades,” ASME J. Turbomachinery, Vol. 117, pp. 133-141.

[22] Hancock, P. E., Bradshaw, P., 1983, “The Effect of Freestream Turbulence on Turbulent Boundary Layers,” ASME J. Fluids Engineering, Vol. 105, pp. 284-289.

[23] Blair, M. F., 1983, “Influence of Free-stream Turbulence on Turbulent Boundary Layer Heat Transfer and Men Profile Development, Part II - Analysis of Results,” ASME J. Heat Transfer, Vol. 105, pp. 41-47.

[24] Krishnamoorthy, V., Sukhatme, S. P., 1989, “The Effect of Freestream Turbulence on Gas Turbine Blade Heat Transfer,” ASME J. Turbomachinery, Vol. 111, pp 497-501.

[25] Jones, T. V., Schultz, D. L., and Hendley, A. D. 1973, “On the Flow in an Isentropic Light Piston Tunnel,” MoD (Proc Exec), Aeronautical Research Council R&M No. 3731.

[26] Goodisman, M. I., Oldfield, M. L. G., Kingcombe, R. C., Jones, T. V., Ainsworth, R. W., and Brooks, A. J., 1992, “An Axial Turbobrake,” ASME J. of Turbo., Vol. 114, No. 2, pp. 419–425.

[27] Hilditch, M. A., Fowler, A., Jones, T. V., Chana, K. S., Oldfield, M. L. G., Ainsworth, R. W., et al. 1994, “Installation of a Turbine Stage in the Pyestock Isentropic Light Piston Facility,” ASME paper no. 94-GT-277.

[28] Povey, T., Chana, K. S., Jones, T. V., and Oldfield, M. L. G., 2003, “The Design and Performance of a Transonic Flow Deswirling System: An Application of Current CFD Design Techniques Tested Against Model and Full-Scale Experiments, Advances of CFD in Fluid Machinery Design,” IMechE Professional Engineering, pp. 65–94.

[29] Qureshi, I., Povey, T., 2011, “A Combustor-Representative Swirl Simulator for a Transonic Turbine Research Facility,” Proc. IMechE, Part G: J. Aerospace Engineering, 2011.

[30] Oldfield, M. L. G., Burd, H. J., Doe, N. G. 1984, “Design of wide-bandwidth analogue circuits for heat transfer instrumentation in transient tunnels. Heat and mass transfer in rotating machinery,” (A86-24451 09-34). Washington, DC, Hemisphere Publishing Corp., 1984, p. 233-258.

[31] Oldfield, M. L. G., Jones, T. V., Schultz, D. L. 1978, “On-Line Computer for Transient Turbine Cascade Instrumentation,” IEEE Transactions on Aerospace and Electronic Systems. Vol. AES-14, No. 5.

[32] Doorly, J. E., Oldfield, M. L. G., 1987, “The Theory of Advanced Multi-Layer Thin Film Heat Transfer Gauges,” Int. J. Heat Mass Transfer. Vol. 30, No. 6, pp. 1159-1168.

[33] Moss, R. W., Ainsworth, R. W. 1993, “A Transient Measurement Technique for Heat Transfer to Metallic Aerofoils,” Proceedings of Eurotherm 32 Seminar, pp. 63-73.

[34] Povey, T., 2003, "On Advances in Annular Cascade Techniques," D.Phil Thesis, Department of Engineering Science, University of Oxford.

[35] Moinier, P., and Giles, M. B., 1998, “Preconditioned Euler and Navier-Stokes Calculations on Unstructured Grids,” Proc. 6th ICFD Conference on Numerical Methods for Fluid Dynamics. Oxford, UK.

[36] Moinier, P., Mueller, J.-D., and Giles, M. B., 2001, “Edgebased Multigrid and Preconditioning for Hybrid Grids,” AIAA Journal, 40(10).

[37] Martinelli, L., 1987, “Calculations of Viscous Flows with a Multigrid Method,” PhD Thesis, Dept. of Mech. And Aerospace Eng., Princeton University, USA.

[38] Mueller, J.-D., and Giles, M. B., 1998, “Edge-Based Multigrid Schemes for Hybrid Grids,” Proc. 6th ICFD Conference on Numerical Methods for Fluid Dynamics. Oxford, UK.

[39] Chana, K. S., 1992, "Heat Transfer and Aerodynamics of a High Rim Speed Turbine Nozzle Guide Vane with Profile End Walls," ASME Paper Number 92-GT-243.

[40] Beard, P. F., 2010, "On Transient Turbine Efficiency Measurements with Engine Representative Inlet Flows," D.Phil Thesis, Department of Engineering Science, University of Oxford.